Ternary chalcogenides $Cs_2Zn_3Se_4$ and $Cs_2Zn_3Te_4$: Potential *p*-type transparent conducting materials

Hongliang Shi, Bayrammurad Saparov, David J. Singh, Athena S. Sefat, and Mao-Hua Du*
Materials Science and Technology Division, Oak Ridge National Laboratory, Oak Ridge, Tennessee 37831, USA
(Received 28 August 2014; published 11 November 2014)

We report the prediction of two ternary chalcogenides that can potentially be used as *p*-type transparent conductors along with experimental synthesis and initial characterization of these compounds, $Cs_2Zn_3Ch_4$ (Ch = Se,Te). In particular, the structures are predicted based on density functional calculations and confirmed by experiments. Phase diagrams, electronic structure, optical properties, and defect properties of $Cs_2Zn_3Se_4$ and $Cs_2Zn_3Te_4$ are calculated to assess the viability of these materials as *p*-type transparent conducting materials (TCMs). $Cs_2Zn_3Se_4$ and $Cs_2Zn_3Te_4$, which are stable under ambient air, display large optical band gaps (calculated to be 3.61 and 2.83 eV, respectively) and have small hole effective masses (0.5–0.77m_e) that compare favorably with other proposed *p*-type TCMs. Defect calculations show that undoped $Cs_2Zn_3Se_4$ and $Cs_2Zn_3Te_4$ are *p*-type materials. However, the free hole concentration may be limited by low-energy native donor defects, e.g., Zn interstitials. Nonequilibrium growth techniques should be useful for suppressing the formation of native donor defects, thereby increasing the hole concentration.

DOI: 10.1103/PhysRevB.90.184104 PACS number(s): 71.20.Nr, 61.72.J−, 78.20.Ci

I. INTRODUCTION

Transparent conducting materials (TCMs) are widely applied as transparent electrodes for solar cells, displays, and light emitting diodes [1,2]. Availability of both *n*- and *p*-type TCMs is essential for the development of transparent electronics. A good TCM must allow high optical transmittance across a wide optical spectrum, requiring a large optical band gap (>3.1 eV) and have high conductivity. Oxides have been extensively studied as TCMs owing to their large band gaps and good chemical stability. At present, several materials are known to be good *n*-type transparent conducting oxides (TCOs), i.e., In_2O_3, SnO_2, and ZnO when suitably doped. The conductivity of commercially available indium tin oxide (In_2O_3:Sn) is close to 10^4 S/cm with electron concentrations as high as 2×10^{21} cm^{-3} [3]. In contrast, *p*-type TCOs are generally plagued by poor hole conductivities, usually 2–3 orders of magnitudes lower than the best electron conductivities in *n*−TCOs. This is caused by (1) fundamental limitations on the hole mobility in valence bands composed of localized O 2*p* orbitals; and (2) the difficulty in *p*-type doping of most oxides due to the low-lying O 2*p* orbitals—high energy is needed to create holes in the valence band, which then often leads to formation of compensating defects. Here, we report on two compounds that may mitigate these problems. The identification of these compounds was based on observations about the existing *p*-type TCMs, and so we begin with a discussion of those materials.

Many materials have been investigated as potential *p*-type TCMs. Several material design approaches have been developed to mitigate the problem of poor hole conductivity due to the localized O 2*p* orbitals. One approach is looking for oxides with cations that introduce occupied cation *d* or *s* states near O-2*p* derived valence band [1,4]. The resulting *p*-*d* and *p*-*s* coupling enhances cation-anion hybridization and increases valence band dispersion. The most notable example of this type of material is Cu-based oxides, such as delafossite $CuMO_2$ (M = Al, Ga, In, Y, Sc, Cr, B, etc.) [1,5–16], and $SrCu_2O_2$ [17]. These materials mix low-gap (2.17 eV [18]) *p*-type semiconductor Cu_2O with large-gap oxides to form ternary oxides. Due to the high-lying Cu-3*d* orbitals, the valence band of these materials is a combination of Cu-3*d* and O-2*p* states, which enhances hybridization and valence band dispersion. The problem with applications of such Cu-based materials comes from the fact that Cu^+ is easily oxidized to Cu^{2+}, thereby trapping a hole on Cu [19], and also some of the compounds tend to take up O in air. The hole transport in delafossite $CuMO_2$ is usually polaronic in nature [20,21]. The highest reported hole conductivity in Cu-based *p*-type TCOs is 220 S/cm observed in Mg-doped $CuCrO_2$ [10]. Ag, Mn, Co, Ir, and Rh-based transition metal oxides have also been studied motivated by related concepts of mixing transition-metal *d* states with O-2*p* states to enhance hybridization [22–27]. The hole effective masses of these transition metal oxides are generally heavy (>2 m_e, where m_e is the electron rest mass) compared to the electron effective mass of <0.3 m_e in *n*-type TCOs [4]. The heavy hole effective mass ultimately limits hole conductivity in these transition metal oxides.

Cation *s* states are generally more delocalized than *d* states, and their hybridization with O-2*p* states can result in lighter hole effective mass. This can be realized in oxides containing ns^2 cations, which have outer electron configuration of ns^2 (e.g., Sn^{2+} and Pb^{2+}). Several such oxides with hole effective masses <0.5 m_e, such as $A_2Sn_2O_3$ (A = K, Na), have been suggested as potentially useful *p*-type TCOs based on first-principles calculations [4]. However, the band gaps of $A_2Sn_2O_3$ are lower than 3 eV and therefore limit their transparency to visible light.

Besides exploring the cation-O interaction to enhance valence band dispersion, the effect of introducing additional anions (e.g., chalcogens [28], halogens, etc.) in oxides has also been investigated. In these materials, oxygen ions often play minor roles in hole transport. A recent theoretical study suggested several such oxides (e.g., B_6O, ZrOS) as promising *p*-type TCOs [4]. (In B_6O, the hole transport is through the B_{12} icosahedron network [4,29].)

*mhdu@ornl.gov

Most of the work on mixed-anion *p*-type TCMs has been focused on layered compounds such as LaCuChO (Ch = S, Se) [30–33]. LaCuChO have alternating $[Cu Ch]^-$ and $[LaO]^+$ layers. The hole transport is through the chalcogenide layer $[Cu Ch]^-$, whereas the $[LaO]^+$ layer is insulating but can modulate the band gap and accommodate *p*-type dopants without strongly scattering holes in the $[Cu Ch]^-$ layer. The $[LaO]^+$ layer can be replaced with a $[BaF]^+$ layer, forming BaCuChF, in which the oxygen ion is entirely eliminated [34–37]. Mg-doped LaCuOSe has been reported to exhibit a high conductivity of 910 S/cm, a hole concentration $>10^{21}$ cm^{-3}, and hole mobility of 3.5 cm^2 V^{-1} s^{-1} [32]. However, the band gap of LaCuOSe is a little too low at 2.8 eV. Layered oxysulfide $[Cu_2S_2][Sr_3Sc_2O_5]$ has a band gap of 3.1 eV and has been reported to have a high hole mobility of 150 cm^2 V^{-1}s^{-1} at room temperature (hole density $\sim 10^{17}$ cm^{-3}) [38]. But high carrier density and high conductivity in this material have not been reported.

In the layered mixed-anion materials discussed above, the valence band is made up of mixed Cu-3*d* and chalcogen *p* states. The calculated hole effective masses along the Γ-M direction for LaCuOSe ($E_g = 2.8$ eV) and $[Cu_2S_2][Sr_3Sc_2O_5]$ ($E_g = 3.1$ eV) are 0.30 m_e [33] and 0.96 m_e [39], respectively. These hole effective masses are much lighter than those of Cu-based delafossites ($>2m_e$) due to the more delocalized chalcogen *p* states. However, the conductivity in the direction perpendicular to the layer is poor due to the presence of the barrier layer (i.e., $[LaO]^+$ or $[BaF]^+$ layer).

Here, we use computational modeling to design layered chalcogenides with more isotropic transport properties as potential *p*-type TCMs. There are several reports of computational materials design of *p*-type TCOs, which screened a large number of oxides in Inorganic Crystal Structure Database (ICSD) (http://fiz-karlsruhe.de/icsd.html) using a first-principles computational approach [4,23]. In this paper, we go beyond existing compounds in ICSD to design additional ternary chalcogenide materials. Note that high throughput first-principles calculations have been previously used to discover previously unknown compounds [40,41]. Our approach, in contrast, is a top-down approach, based on rational design combined with both first-principles calculations and experiments.

Hole mobilities of ZnSe and ZnTe have been reported to be as high as 50 cm^2 V^{-1} s^{-1} (Ref. [42]) and 340 cm^2 V^{-1} s^{-1} (Ref. [43]) in low-hole-density samples at room temperature. For comparison, the electron mobility of In_2O_3, which is the best *n*-type TCO, has been reported to be as high as 200 cm^{2}V^{-1}s^{-1} at room temperature [44]. The band gaps of ZnSe and ZnTe are 2.82 eV and 2.39 eV, respectively, which are too low for TCMs. Androulakis *et al.* [45] pointed out that the band gap of HgCh (Ch = S, Se, Te) (zero gap matetials) can be increased by a dimensional reduction approach, in which the cubic HgCh structure is reduced to lower dimension structures by admixing with Cs_2Ch. For example, the band gap increases from HgSe (0 eV, 3D structure) to $Cs_2Hg_6Se_7$ (1.0 eV, open framework 3D), $Cs_2Hg_3Se_4$ (2.1 eV, 2D), Cs_2HgSe_2 (3.0 eV, 1D chain), and Cs_6HgSe_4 (>4 eV, 0D, molecular units). Similarly, the band gap increases from 1.48 eV for CdTe to 2.5 eV for $Cs_2Cd_3Te_4$. The approach of dimensional reduction increases the band gap at the expense of decreasing the band dispersion due to weakened covalent bonding and consequently narrower bands. The 2D-layered structure may be a reasonable compromise between the band gap and the band dispersion when designing new *p*-type TCMs. Mixing ZnCh with Cs_2Ch (Ch = Se, Te) in 6:1 or 3:1 ratio to form $Cs_2Zn_6Ch_7$ or $Cs_2Zn_3Ch_4$, respectively, may raise the band gap to values above 3 eV. However, $Cs_2Zn_6Ch_7$ is not chemically stable (discussed in Sec. III A), and the syntheses of $Cs_2Zn_3Ch_4$ (Ch = Se, Te) have not been reported in the literature. Since the analogs of $Cs_2Zn_3Se_4$ and $Cs_2Zn_3Te_4$ (e.g., $Cs_2Zn_3S_4$ [46] and $(Rb,Cs)_2Cd_3Te_4$ [47]) do exist, we use density functional calculations to predict the structures of $Cs_2Zn_3Se_4$ and $Cs_2Zn_3Te_4$ and further study chemical stability, electronic structure, optical properties, and defect properties of $Cs_2Zn_3Se_4$ and $Cs_2Zn_3Te_4$ to assess their viability as *p*-type TCMs. Experimental syntheses have also been performed.

II. METHODS

We calculated the electronic structure, optical absorption, phase diagram, and defect properties of $Cs_2Zn_3Se_4$ and $Cs_2Zn_3Te_4$ based on density functional calculations. Perdew, Burke, and Ernzerhof (PBE) generalized gradient approximation (GGA) [48] was used to calculate the band structures. The band gap and the optical absorption coefficients were calculated using PBE [46], Heyd, Scuseria, and Ernzerhof (HSE) [49], and Tran-Blaha modified Becke-Johnson potential functional (TB-mBJ) [50–52] functionals. In HSE calculations, a 36% Fock nonlocal exchange was used because it reproduced band gaps of ZnSe, ZnTe, and K_2ZnTe_2 very well [2.78 eV, 2.23 eV, and 3.13 eV (calculated) vs 2.82 eV, 2.39 eV, and 3.0 eV [53] (experimental) for ZnSe, ZnTe, and K_2ZnTe_2, respectively]. The TB-mBJ is a recently developed functional that has been shown to give good band gaps and optical properties for many semiconductors and insulators but requires a much lower computational cost compared to HSE calculations. Optical absorption coefficients were calculated on a primitive cell of $Cs_2Zn_3Ch_4$ (two formula units) using a $4 \times 4 \times 4$ k-point mesh in HSE and PBE calculations and a $8 \times 8 \times 8$ k-point mesh in TB-mBJ calculations. The PBE functionals were used to calculate the phase diagram and defect formation energies. Defect calculations were performed using a supercell of eight formula units of $Cs_2Zn_3Ch_4$ and a $2 \times 2 \times 2$ k-point mesh.

Spin-orbit coupling was included in the calculations of the electronic structure and optical properties, but not in the calculations of the phase diagram and defect properties, because the spin-orbit coupling mainly affects the electronic structure but not structures and total energy differences, at least for elements of moderately heavy mass [the heaviest elements here are Cs ($Z = 55$) and Te ($Z = 52$)] [54,55].

The PBE and HSE calculations were performed using the Vienna *Ab initio* Simulation Package (VASP) [56,57]. The electron and core interactions are included using the frozen-core projected augmented wave approach [54]. The Zn 3*d* electrons are explicitly treated as valence electrons. The valence wave functions were expanded in a plane-wave basis with a cutoff energy of 400 eV. All the atoms were relaxed by minimizing the Feynman-Hellmann forces less

than 0.01 eV/ Å. The TB-mBJ calculations were performed using the general linearized augmented plane-wave (LAPW) method, as implemented in the WIEN2K code [58]. These are all electron calculations. The WIEN2k calculations were performed using well converged LAPW basis sets plus local orbitals to treat semicore states. The muffin-tin sphere radii employed were 2.5 Bohr, 2.3 Bohr, and 2.3 Bohr for Cs, Zn, and Se, respectively, in $Cs_2Zn_3Se_4$ and 2.5 Bohr, 2.4 Bohr, and 2.55 Bohr for Cs, Zn, and Te, respectively, in $Cs_2Zn_3Te_4$. The size of the LAPW sector of the basis corresponded to $R_{MT}K_{max} = 9.0$, where R_{MT} is the smallest sphere radius and K_{max} is the plane wave cutoff.

For defect calculations, the formation energy of a defect in the charge state q is given by

$$\Delta H_{D,q}(\varepsilon_f, \Delta\mu_\alpha) = (E_{D,q} - E_H) - \sum_\alpha n_\alpha\left(\Delta\mu_\alpha + \mu_\alpha^{\text{ref}}\right) + q(\varepsilon_{\text{VBM}} + \varepsilon_f). \quad (1)$$

In the first term, $E_{D,q}$ and E_H are the total energies of the supercells that contain the defect and that of the defect-free host material, respectively. n_α is the difference in the number of atoms for the αth atomic species between the defect-containing and defect-free supercells. $\Delta\mu_\alpha$ is the chemical potential for the αth atomic species, relative to μ_α^{ref}, which is taken as the chemical potential of the αth atomic species in its elemental bulk form. ε_f is the Fermi energy referenced to the valence band maximum (VBM), ε_{VBM}. The transition level of a defect, $\varepsilon(q/q')$, corresponding to a change in its charge state between q and q', is given by the Fermi level, at which the formation energies, $\Delta H(q)$ and $\Delta H(q')$, for charge states q and q' are equal to each other:

$$\varepsilon(q/q') = [\Delta H(q) - \Delta H(q')]/(q' - q). \quad (2)$$

In the defect calculations, the VBM and the conduction band minimum (CBM) from PBE calculations were corrected using the band gaps obtained from the HSE calculations. For this purpose, the common reference energy in the PBE and HSE calculations were chosen as the average electrostatic potential in the supercell. The shallow defect levels, which mainly have the character of bulk electronic states, were shifted with their respective band edges, while the deep levels, which are highly localized, were not corrected since they are not expected to move following the band gap correction. Details of these commonly used correction schemes can be found, for example, in Ref. [59]. Corrections to the defect formation energy due to potential alignment (between the host and a charged defect supercell), band filling effects, and image charge correction [56,60] were applied wherever appropriate.

III. RESULTS

New p-type transparent conducting ternary chalcogenides ($Cs_2Zn_3Se_4$ and $Cs_2Zn_3Te_4$) are predicted by theory. We take the material design approach that existing binary compounds with good hole mobility (ZnSe and ZnTe) are modified through admixing with highly electropositive cations and adopt a dimensionally reduced structure such that the band gap is significantly increased while retaining highly dispersive valence bands in all three dimensions. The calculated crystal structure, phase diagram, electronic structure, optical properties, and defect properties along with the experimental syntheses are presented in this section.

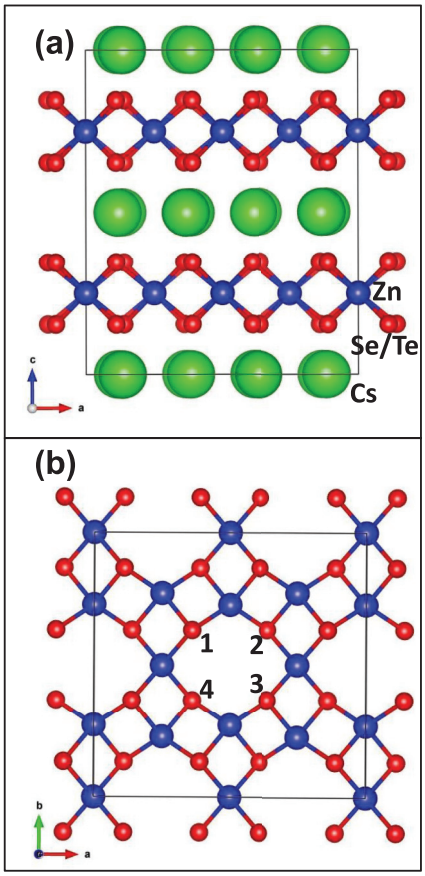

FIG. 1. (Color online) (a) Crystal structure of $Cs_2Zn_3Se_4$ ($Cs_2Zn_3Te_4$) featuring $[Zn_3Se_4]^{2-}$ ($[Zn_3Te_4]^{2-}$) layers stacked along the c axis and Cs^+ cations acting as spacers between the layers. (b) $[Zn_3Se_4]^{2-}$ ($[Zn_3Te_4]^{2-}$) layer in $Cs_2Zn_3Se_4$ ($Cs_2Zn_3Te_4$) viewed along [001]. The green, blue, and red atoms are Cs, Zn, and Se/Te, respectively.

A. Crystal structures of $Cs_2Zn_3Se_4$ and $Cs_2Zn_3Te_4$

To our knowledge, crystal structures of $Cs_2Zn_6Ch_7$ and $Cs_2Zn_3Ch_4$ (Ch = Se, Te) have not been reported in the literature. We adopted the structures of the existing compounds $Cs_2Hg_6S_7$ [61] and $Cs_2Cd_3Ch_4$ [45] for $Cs_2Zn_6Ch_7$ and $Cs_2Zn_3Ch_4$, respectively. $Cs_2Zn_3Ch_4$ is found to be stable against decomposition to Cs_2Ch and $ZnCh$, whereas $Cs_2Zn_6Ch_7$ is unstable against decomposition to $Cs_2Zn_3Ch_4$ and $ZnCh$ and therefore is not further studied. Details of the phase diagram for $Cs_2Zn_3Ch_4$ are shown in Sec. III B.

Figure 1(a) shows the crystal structure of $Cs_2Zn_3Ch_4$, which has alternating $[Zn_3Ch_4]^{2-}$ and Cs^+ layers stacked along the [001] direction (space group *Ibam*, No. 72). The PBE optimized lattice parameters and atomic coordinates for $Cs_2Zn_3Se_4$ and $Cs_2Zn_3Te_4$ are shown in Tables I and II. The $[Zn_3Ch_4]^{2-}$ layer consists of edge-sharing $ZnCh_4$ tetrahedra, as shown in Fig. 1(b). Each chalcogen ion in the $[Zn_3Ch_4]^{2-}$ layer is at the corner of four tetrahedra. Three of them are $ZnCh_4$ tetrahedra, and one is a Ch_4 tetrahedron with a vacancy

TABLE I. Lattice parameters for $Cs_2Zn_3Se_4$ and $Cs_2Zn_3Te_4$ (space group *Ibam*, No. 72) optimized using PBE calculations. The lattice parameters in parentheses are the experimental results.

	$Cs_2Zn_3Se_4$	$Cs_2Zn_3Te_4$
a (Å)	6.143 (6.023)	6.536 (6.411)
b (Å)	11.984 (11.777)	12.910 (12.668)
c (Å)	14.634 (14.352)	15.517 (15.243)

at the center. For example, the four chalcogen ions in Fig. 1(b) (labeled by 1–4) form a tetrahedron with a vacancy at the center. These vacancies result in "holes" in the $[Zn_3Ch_4]^{2-}$ layer, as can be seen in Fig. 1(b). Filling these vacancies with Zn would result in a ZnCh layer that has the same structure as the $[CuCh]^-$ layer in LaCuOCh.

B. Phase diagrams of $Cs_2Zn_3Se_4$ and $Cs_2Zn_3Te_4$

Under thermal equilibrium conditions for crystal growth, the chemical potential $\Delta\mu_\alpha$ in Eq. (1) must meet several conditions in order to maintain the stable growth of the crystal and avoid competing phases. These conditions are shown below for $Cs_2Zn_3Se_4$ as an example.

(i) To maintain the stability of a compound during crystal growth, the sum of the chemical potentials of its constituent elements must be equal to the heat of formation, $\Delta H(Cs_2Zn_3Se_4)$, of the compound, i.e.,

$$2\Delta\mu_{Cs} + 3\Delta\mu_{Zn} + 4\mu_{Se} = \Delta H(Cs_2Zn_3Se_4) = -9.94\text{eV}. \quad (3)$$

Note that all calculated heats of formation of ternary and binary compounds in this paper are given for per formula unit.

(ii) To avoid precipitation of Cs, Zn, and Se, $\Delta\mu_\alpha$ are bound by

$$\Delta\mu_{Cs} \leqslant 0, \ \Delta\mu_{Zn} \leqslant 0, \ \Delta\mu_{Se} \leqslant 0. \quad (4)$$

(iii) To avoid the formation of competing phases, chemical potentials are limited by

$$\begin{aligned} 2\Delta\mu_{Cs} + \Delta\mu_{Se} &\leqslant \Delta H(Cs_2Se) = -2.940 \text{ eV}, \\ 2\Delta\mu_{Cs} + 3\Delta\mu_{Se} &\leqslant \Delta H(Cs_2Se_3) = -4.940 \text{ eV}, \\ \Delta\mu_{Zn} + \Delta\mu_{Se} &\leqslant \Delta H(ZnSe) = -2.029 \text{ eV}, \end{aligned} \quad (5)$$

TABLE II. Atomic coordinates for $Cs_2Zn_3Se_4$ and $Cs_2Zn_3Te_4$ optimized using PBE calculations. The lattice parameters in parentheses are the experimental results.

Atom	Wyckoff site	x	y	z
Cs	8j	0.2332 (0.2319)	0.3783 (0.3794)	0.5 (0.5)
Zn1	4a	0.5 (0.5)	0.5 (0.5)	0.25 (0.25)
Zn2	8g	0.0 (0.0)	0.2721 (0.2719)	0.25 (0.25)
Se	16k	0.2793 (0.2764)	0.3671 (0.3682)	0.1544 (0.1524)
Cs	8j	0.2304 (0.232)	0.3774 (0.3779)	0.5 (0.5)
Zn1	4a	0.5 (0.5)	0.5 (0.5)	0.25 (0.25)
Zn2	8g	0.0 (0.0)	0.27 (0.2683)	0.25 (0.25)
Te	16k	0.2765 (0.2717)	0.3683 (0.37)	0.1518 (0.1495)

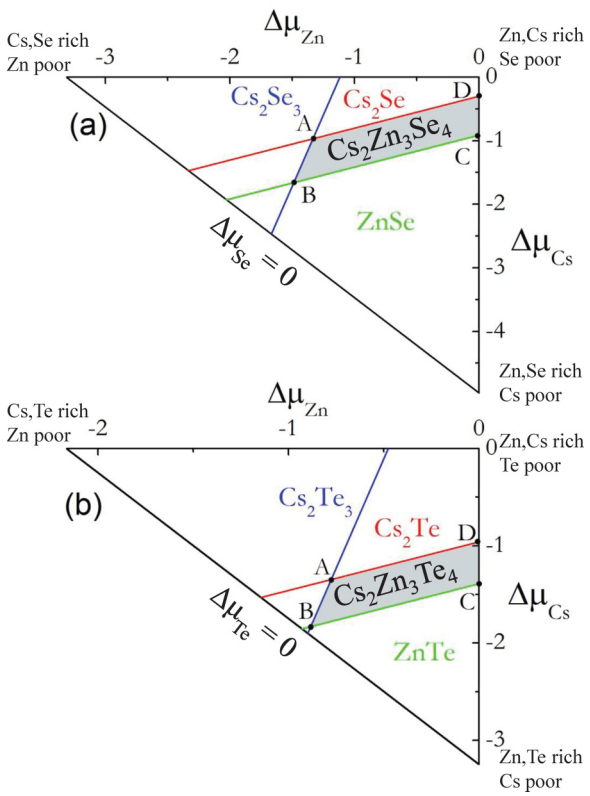

FIG. 2. (Color online) Calculated phase diagrams for $Cs_2Zn_3Se_4$ (a) and $Cs_2Zn_3Te_4$ (b). The stable regions for $Cs_2Zn_3Se_4$ and $Cs_2Zn_3Te_4$ are shaded.

where $\Delta H(Cs_2Se)$, $\Delta H(Cs_2Se_3)$, and $\Delta H(ZnSe)$ are the heats of formation for Cs_2Se, Cs_2Se_3, and ZnSe, respectively.

Equations (3)–(5) determine the phase diagram of $Cs_2Zn_3Se_4$, which is shown in Fig. 2(a) as a two-dimensional panel with two independent variables, $\Delta\mu_{Cs}$ and $\Delta\mu_{Zn}$. The stable region for $Cs_2Zn_3Se_4$ in the phase diagram is shown as the shaded trapezoid in Fig. 2(a).

Similar to $Cs_2Zn_3Se_4$, the chemical potentials for $Cs_2Zn_3Te_4$ satisfy conditions as follows:

$$\begin{aligned} &2\Delta\mu_{Cs} + 3\Delta\mu_{Zn} + 4\mu_{Te} = \Delta H(Cs_2Zn_3Te_4) = -6.494 \text{ eV}, \\ &\Delta\mu_{Cs} \leqslant 0, \ \Delta\mu_{Zn} \leqslant 0, \ \Delta\mu_{Te} \leqslant 0, \\ &2\Delta\mu_{Cs} + \Delta\mu_{Te} \leqslant \Delta H(Cs_2Te) = -3.062 \text{ eV}, \\ &2\Delta\mu_{Cs} + 3\Delta\mu_{Te} \leqslant \Delta H(Cs_2Te_3) = -3.799 \text{ eV}, \\ &\Delta\mu_{Zn} + \Delta\mu_{Te} \leqslant \Delta H(ZnTe) = -0.929 \text{ eV}. \end{aligned} \quad (6)$$

The stable region for $Cs_2Zn_3Te_4$ in the phase diagram is shown as the shaded trapezoid in Fig. 2(b). The phase diagrams in Fig. 2 demonstrate that the single-phase $Cs_2Zn_3Se_4$ and $Cs_2Zn_3Te_4$ can be grown.

C. Electronic structure and optical absorption of $Cs_2Zn_3Se_4$ and $Cs_2Zn_3Te_4$

Figure 3 shows the band structures of $Cs_2Zn_3Se_4$ and $Cs_2Zn_3Te_4$ calculated using PBE functionals. The HSE calculations show much larger band gaps than the PBE calculations, as shown in Table III. The TB-mBJ band gap of $Cs_2Zn_3Se_4$

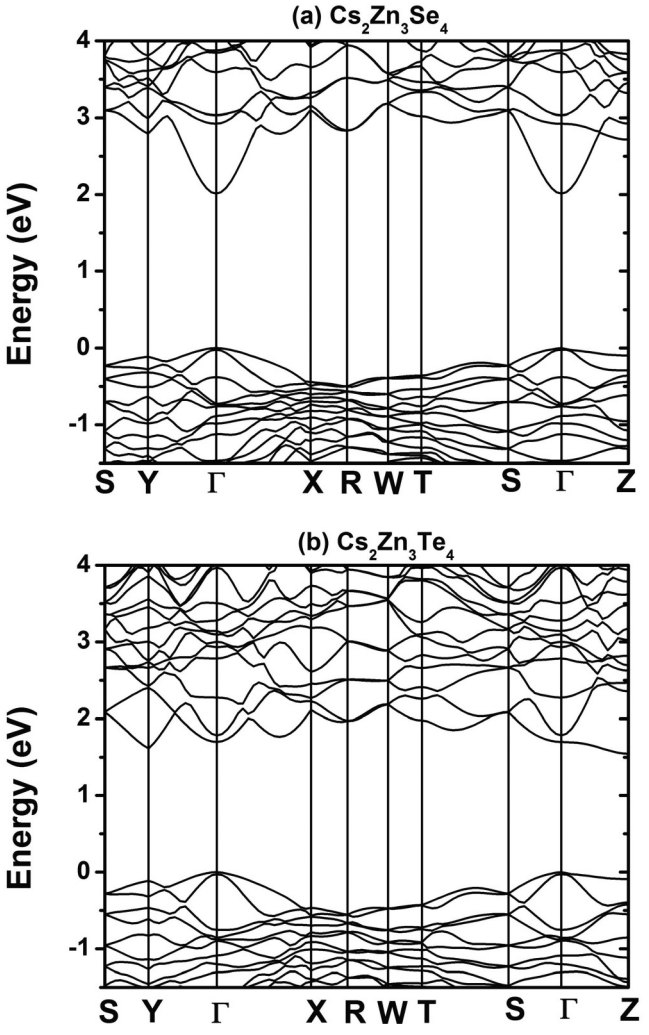

FIG. 3. Band structures of (a) $Cs_2Zn_3Se_4$ and (b) $Cs_2Zn_3Te_4$ calculated using PBE functionals. Spin-orbit coupling is included. Note that the band gaps are underestimated due to the PBE-GGA error.

(3.52 eV) is close to the HSE band gap (3.61 eV). However, the TB-mBJ band gap of $Cs_2Zn_3Te_4$ appears to be too small (2.29 eV). It is much smaller than the HSE band gap of 2.75 eV and is even smaller than the experimental band gap of ZnTe (2.39 eV). This is inconsistent with the expected larger band gap of $Cs_2Zn_3Te_4$ than that of ZnTe as a result of the reduced dimension and the addition of highly electropositive Cs in $Cs_2Zn_3Te_4$. Therefore, the HSE calculation provides a more plausible result for the band gap of $Cs_2Zn_3Te_4$ than the TB-mBJ calculation. Note, however, that in both compounds

TABLE III. Band gaps of $Cs_2Zn_3Se_4$ and $Cs_2Zn_3Te_4$ calculated using PBE, HSE, and TB-mBJ functionals. Spin-orbit coupling is included in the calculations. The units are in eV.

	PBE	HSE	TB-mBJ
$Cs_2Zn_3Se_4$	2.01	3.61	3.52
$Cs_2Zn_3Te_4$ (indirect $\Gamma - Z$)	1.55	2.75	2.29
$Cs_2Zn_3Te_4$ (direct at Z)	1.64	2.83	2.40

TABLE IV. Hole effective masses of the top two valence bands (separated by ~20 meV, see text) in $Cs_2Zn_3Se_4$ and $Cs_2Zn_3Te_4$ calculated using PBE functionals and spin-orbit coupling. The units are in electron rest mass m_e.

	$Cs_2Zn_3Se_4$			$Cs_2Zn_3Te_4$		
	m_h^{xx}	m_h^{yy}	m_h^{zz}	m_h^{xx}	m_h^{yy}	m_h^{zz}
VBM	2.16	1.75	0.65	1.01	2.12	0.55
VBM-1	0.77	0.77	7.01	0.74	0.50	2.59

the TB-mBJ and HSE results for the electronic structure, band gap, and optical properties are relatively similar to each other when compared to the PBE results.

$Cs_2Zn_3Se_4$ has a direct band gap at Γ point, whereas $Cs_2Zn_3Te_4$ has an indirect band gap (VBM at Γ and CBM at Z). The direct band gaps of $Cs_2Zn_3Se_4$ and $Cs_2Zn_3Te_4$ are 3.61 eV and 2.83 eV, respectively, calculated using HSE functionals. The calculated band gap of $Cs_2Zn_3Se_4$ is sufficiently large, whereas that of $Cs_2Zn_3Te_4$ is slightly below the target of >3.1 eV for a TCM. The optical absorption coefficients of $Cs_2Zn_3Se_4$ and $Cs_2Zn_3Te_4$ are calculated using PBE, HSE, and TB-mBJ functionals, as shown in Fig. 4. The onsets of the optical absorption are consistent with the calculated direct band gaps shown in Table III. The general features in the optical absorption coefficients calculated using the three different functionals are in reasonable agreement except for their different band gaps. The TB-mBJ calculations used a denser k-mesh ($8 \times 8 \times 8$) than the HSE and PBE calculations ($4 \times 4 \times 4$) and therefore show smoother absorption curves, especially near the band edge.

The VBM and CBM states of $Cs_2Zn_3Se_4$ ($Cs_2Zn_3Te_4$) primarily have the characters of Se $4p$ (Te $5p$) and Zn $4s$ states, respectively. At Γ point, the VBM state is mainly made up of p_z orbitals of the chalcogen ions, whereas the state next to the VBM in the valence band (VBM-1 state) is mainly of p_x and p_y characters. The calculated energy separations between the VBM and the VBM-1 states at Γ point are only 22 and 25 meV for $Cs_2Zn_3Se_4$ and $Cs_2Zn_3Te_4$ at the PBE level, respectively, and are 16 and 20 meV at the HSE level. These two states are part of light and heavy hole bands along the Γ-X, Γ-Y, and Γ-Z directions, as shown in Fig. 3. Along the Γ-X and Γ-Y directions, the light band (p_x and p_y states) is below the heavy band (p_z states) at the Γ point. Along the Γ-Z directions, the light band (p_z states) is above the heavy band (p_x and p_y states) at the Γ point. Since the energy separation between the light and heavy hole bands is very small (<kT at room temperature), the light hole bands along the Γ-X and Γ-Y directions can be easily populated if the holes are introduced into the valence bands.

The light hole bands along the Γ-X, Γ-Y, and Γ-Z directions are all very dispersive, as shown in Fig. 3. The calculated light hole effective masses for $Cs_2Zn_3Se_4$ and $Cs_2Zn_3Te_4$ are small (0.5–0.77 m_e, see Table IV). Despite having a layered structure, the interaction between the chalcogen ions across the Cs layer is significant. The calculated light hole effective mass along the z direction (m_h^{zz}) is comparable or even smaller than those along the x and y directions (m_h^{xx}

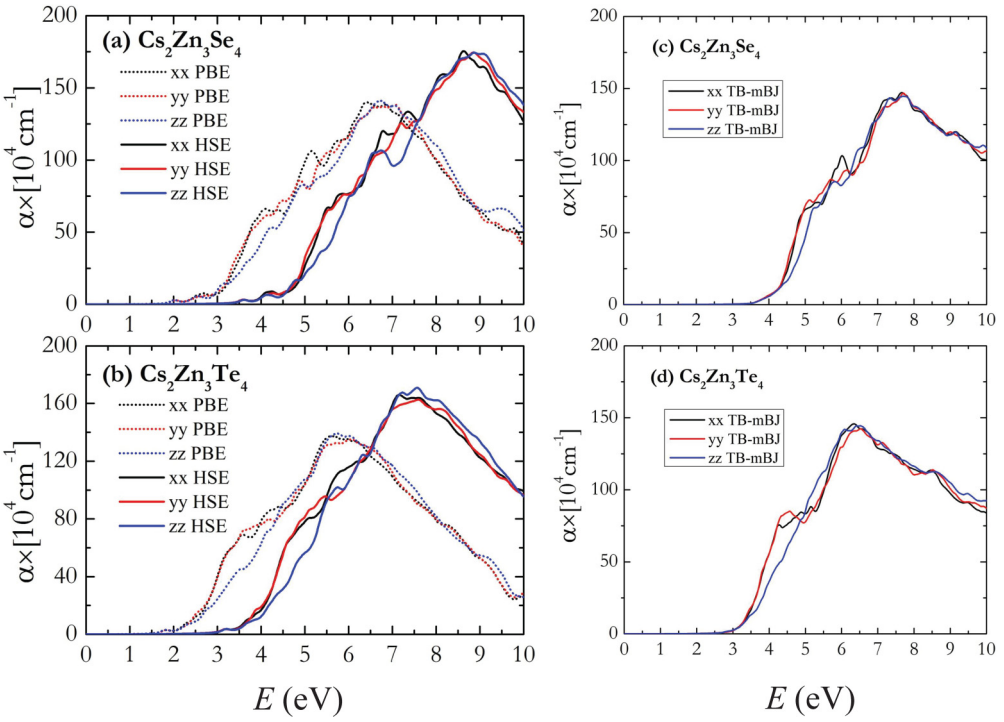

FIG. 4. (Color online) Optical absorption coefficients of (a) $Cs_2Zn_3Se_4$ and (b) $Cs_2Zn_3Te_4$ calculated using both PBE and HSE functionals. Optical absorption coefficients calculated using TB-mBJ functionals are shown in (c) $Cs_2Zn_3Se_4$ and (d) $Cs_2Zn_3Te_4$. Spin-orbit coupling is included.

and m_h^{yy}), as shown in Table IV. This is in sharp contrast to LaCuChO and $[Cu_2S_2][Sr_3Sc_2O_5]$, where the effective mass along the z direction is much larger than those on the ab plane [33,39]. In LaCuChO and $[Cu_2S_2][Sr_3Sc_2O_5]$, the hole conducting $[CuCh]^-$ layers are separated by relatively thick insulating layers (i.e., $[LaO]^+$ in LaCuChO and $[Sr_3Sc_2O_5]^{2+}$ in $[Cu_2S_2][Sr_3Sc_2O_5]$); therefore, the holes only diffuse efficiently on the ab plane. In contrast, the adjacent $[Zn_3Ch_4]^{2-}$ layers in $Cs_2Zn_3Ch_4$ are strongly coupled through a one-atom-thick layer of Cs^+, which results in small hole effective masses along the z direction.

The combination of large band gaps and small effective masses for $Cs_2Zn_3Se_4$ and $Cs_2Zn_3Te_4$ compare favorably with those of other proposed p-type TCMs [4]. The effective masses of $Cs_2Zn_3Se_4$ and $Cs_2Zn_3Te_4$ (0.5-0.77 m_e) are much smaller than those of transition-metal-based p-TCOs, such as cuprates of delafossite structures. Among layered oxychalcogenides, the reported hole effective masses along the Γ-M direction are 0.30 m_e for LaCuOSe ($E_g = 2.8$ eV) [33] and 0.96 m_e for $[Cu_2S_2][Sr_3Sc_2O_5]$ ($E_g = 3.1$ eV) [39]. The hole transport in these materials is 2D in nature since the effective mass along the Γ-Z direction is very large. B_6O has a band gap of 3 eV and a calculated hole effective mass of 0.59 m_e [4]. In comparison, $Cs_2Zn_3Se_4$ has a combination of large band gap (calculated to be 3.61 eV) and small hole effective masses along x, y, and z directions (0.65–0.77m_e), which are superior compared to other proposed p-TCMs.

D. Experimental syntheses

$Cs_2Zn_3Se_4$ and $Cs_2Zn_3Te_4$ crystals were synthesized following the procedure described in the literature [43,45,62]. Large scale (total masses up to 2.5 g) reactions employing a modified Bridgman set up was further carried out, yielding transparent yellow and dark yellow crystals for $Cs_2Zn_3Se_4$ and $Cs_2Zn_3Te_4$, respectively. $Cs_2Zn_3Se_4$ and $Cs_2Zn_3Te_4$ crystals are found to be stable under ambient air. The handling of these crystals does not require the use of glove boxes. Crystallographic data were obtained by single-crystal x-ray diffraction. The experimentally measured lattice parameters and atomic coordinates agree very well with the calculated values (as shown in Tables I and II), confirming the crystal structures predicted by theory. The calculated lattice parameters deviate from the measured ones by less than 2%.

Large amounts of carbon and ZnCh impurities are found in $Cs_2Zn_3Ch_4$ crystals. The weight percentages of the ZnCh impurities are estimated to be 9.9% and 11.04% in $Cs_2Zn_3Se_4$ and $Cs_2Zn_3Te_4$, respectively [63]. Carbon impurities come from the reaction of Cs with carbon coating of the quartz tube. Since part of the carbon coating was breached during syntheses, some Cs was lost to the reaction with the quartz, hence the large amount of ZnCh impurities in $Cs_2Zn_3Ch_4$.

The presence of a large amount of ZnSe (ZnTe) impurities in $Cs_2Zn_3Se_4$ ($Cs_2Zn_3Te_4$) prevents the accurate measurement of the band gap and is responsible for the yellow (dark yellow) color of the crystal. The observed colors of the crystals are consistent with the band gaps of ZnSe (2.82 eV) and ZnTe (2.39 eV).

The attack of Cs on the carbon coating and the quartz tube is the main problem in the preliminary syntheses of $Cs_2Zn_3Se_4$ and $Cs_2Zn_3Te_4$. Better methods of encapsulating reactants are needed in future syntheses.

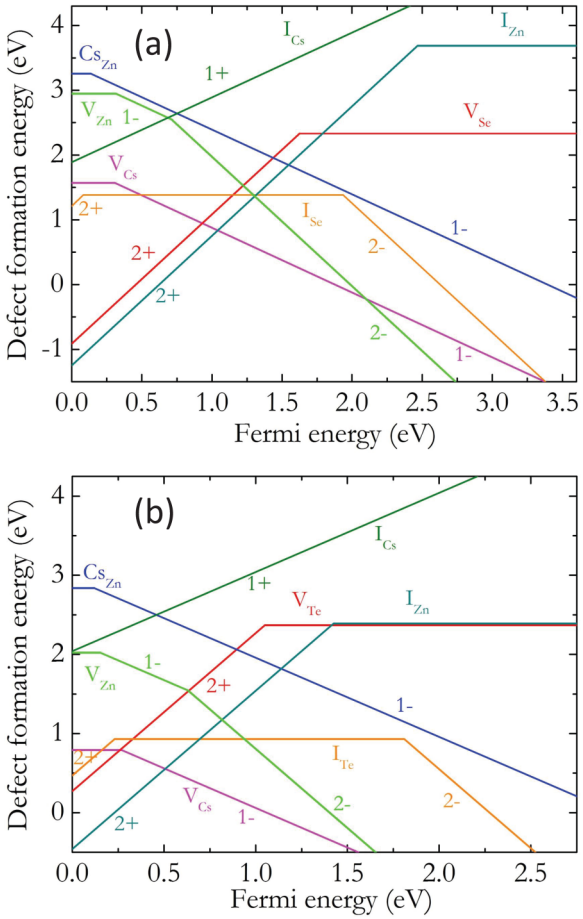

FIG. 5. (Color online) Formation energies of native defects in (a) $Cs_2Zn_3Se_4$ and (b) $Cs_2Zn_3Te_4$ calculated using chemical potentials at the point B in the phase diagram (see Fig. 2), which corresponds to the chalcogen-rich limit. The slope of a formation energy line indicates the charge state of the defect. The Fermi level at which the slope changes is the charge transition level defined by Eq. (2).

E. Native defects in $Cs_2Zn_3Se_4$ and $Cs_2Zn_3Te_4$

Native defects play an important role in hole generation and compensation in p-type TCMs. For example, cation vacancies and anion interstitials (acceptors) typically generate holes and thus are useful native defects in p-TCMs, whereas anion vacancies and cation interstitials (donors) compensate acceptors and therefore are detrimental to the performance of the p-TCMs.

Figure 5 shows the calculated formation energies of native point defects (including vacancies, interstitials, and antisites) in $Cs_2Zn_3Se_4$ and $Cs_2Zn_3Te_4$. The defect formation energies are calculated using chemical potentials at point B in the phase diagram (see Fig. 2), which corresponds to the chalcogen-rich limit. The results show that the dominant native acceptor is Cs vacancy (V_{Cs}), while the main native donors are Zn interstitial (I_{Zn}) and anion vacancy (V_{Se} or V_{Te}). The formation energy of the lowest energy native acceptor (V_{Cs}) crosses that of the lowest energy native donor (I_{Zn}) in the lower part of the band gap for both $Cs_2Zn_3Se_4$ and $Cs_2Zn_3Te_4$. The crossing point pins the Fermi level in the undoped materials. Therefore, the undoped $Cs_2Zn_3Se_4$ and $Cs_2Zn_3Te_4$ should be p-type. P-type doping may further lower the Fermi level. However, the formation energy of I_{Zn} in both $Cs_2Zn_3Se_4$ and $Cs_2Zn_3Te_4$ is very low. It decreases with decreasing Fermi level and becomes negative before the Fermi level reaches the VBM, thereby limiting the free hole concentration in the valence band.

The low energy of I_{Zn} is related to the structure of $Cs_2Zn_3Ch_4$. As discussed in Sec. III A, there are hollow Ch_4 tetrahedra in the $[Zn_3Ch_4]^{2-}$ layer. For example, the four chalcogen ions in Fig. 1(b) (labeled by 1–4) form a tetrahedron with a vacancy at the center. These vacancies provide near-perfect sites for Zn interstitials, each of which can form four Zn-Ch bonds, resulting in a low formation energy. The low coordination number (3) of the Ch ion in the Zn-deficient $[Zn_3Ch_4]^{2-}$ layer also leads to low formation energy for the Ch vacancy, which is also an important native donor defect.

IV. DISCUSSION

$Cs_2Zn_3Ch_4$ proposed in this paper has a layered structure with alternating cation (Cs^+) and anion ($[Zn_3Ch_4]^{2-}$) layers, similar to the layered oxychalcogenides such as LaCuOCh, which have alternating $[LaO]^+$ and $[CuCh]^-$ layers. In Cu-based layered oxychalcogenides, the valence band is made up of hybridized Cu-3d and chalcogen p states. Such hybridization raises the VBM and reduces the band gap. $Cs_2Zn_3Se_4$ and $Cs_2Zn_3Te_4$ proposed in this paper do not have Cu, which contributes to their larger band gaps. However, replacing Cu with Zn requires a Zn-deficient $[Zn_3Ch_4]$ layer to restore the charge of the layer. This results in Zn vacancy sites that are perfect for accommodating Zn interstitials (native donors) and causes a problem for p-type doping, as shown in Sec. III E. This problem highlights the difficulty of increasing the band gap without introducing compensating native defects [64].

Adopting chalcogen-rich conditions during crystal growth and using postgrowth annealing under chalcogen vapor can suppress the formation of I_{Zn} and V_{Ch}. However, the calculated defect formation energies show that even at the chalcogen-rich limit (point B in the phase diagram in Fig. 2), the Fermi level cannot be lowered to the VBM by p-type doping due to the spontaneous formation of native donor defects (e.g., I_{Zn}) when their formation energies become negative (see Fig. 5). Further increasing the chalcogen chemical potential beyond that at point B in Fig. 2 would lead to the formation of chalcogen-rich phases, such as Cs_2Ch_3. Therefore, nonequilibrium growth should be the key to allow higher chalcogen chemical potential without forming the chalcogen-rich secondary phases, thereby suppressing the formation of native donor defects (i.e., I_{Zn} and V_{Ch}) [65–68].

Low-temperature non-equilibrium growth techniques such as molecular beam epitaxy and metalorganic chemical vapor deposition have been shown to significantly increase the dopant concentration over solid solubility without forming secondary phases [69,70]. In nonequilibrium growth methods, the chemical potentials of constituent elements can be moved beyond thermal-equilibrium phase boundaries without forming secondary phases because thermal equilibrium cannot be reached at low growth temperatures, and surface kinetics prevents atomic migration and formation of secondary phases

[65–68]. The same approach can be applied to managing native defects in semiconductors. Under low-temperature non-equilibrium growth conditions, it is possible to obtain chalcogen-rich and Zn-poor conditions beyond the thermal-equilibrium phase boundaries for $Cs_2Zn_3Ch_4$ while not forming chalcogen-rich phases (e.g., Cs_2Ch_3). This should suppress the formation of native donor defects (e.g., Zn interstitial) and further lower the Fermi level towards the valence band.

V. CONCLUSIONS

We predict ternary chalcogenide compounds, $Cs_2Zn_3Se_4$ and $Cs_2Zn_3Te_4$, as potential *p*-type TCM based on design rules and first-principles calculations, followed by successful experimental synthesis and early characterization. Structures of $Cs_2Zn_3Se_4$ and $Cs_2Zn_3Te_4$ are predicted based on density functional calculations and confirmed by experiments. $Cs_2Zn_3Se_4$ and $Cs_2Zn_3Te_4$ are stable under ambient air and display large optical band gaps (calculated to be 3.61 and 2.83 eV, respectively). The band gap of $Cs_2Zn_3Se_4$ is sufficiently large for a TCM, whereas that of $Cs_2Zn_3Te_4$ is slightly below the target of >3.1 eV. Despite having layered structures, the light hole effective masses of $Cs_2Zn_3Se_4$ and $Cs_2Zn_3Te_4$ are calculated to be small in all three dimensions (0.5–0.77 m_e). Strong hybridization between the $[Zn_3Ch_4]$ layers across the one-atom-thick Cs layer leads to highly dispersive valence band in the Γ-Z direction. The combination of large band gaps and small hole effective masses of $Cs_2Zn_3Se_4$ and $Cs_2Zn_3Te_4$ compare favorably with other proposed *p*-type TCMs. Defect calculations show that undoped $Cs_2Zn_3Se_4$ and $Cs_2Zn_3Te_4$ are *p*-type materials. However, the free hole concentration may be limited by low-energy native donor defects, e.g., Zn interstitials. Nonequilibrium growth techniques should be useful for suppressing the formation of native donor defects, thereby increasing the hole concentration.

ACKNOWLEDGMENTS

This paper was supported by the Department of Energy, Basic Energy Sciences, Materials Sciences and Engineering Division.

[1] H. Kawazoe, H. Yanagi, K. Ueda, and H. Hosono, MRS Bulletin **25**, 28 (2000).
[2] S. Sheng, G. Fang, C. Li, S. Xu, and X. Zhao, Phys. Stat. Sol. (a) **203**, 1891 (2006).
[3] I. Hamberg and C. G. Granqvist, J. Appl. Phys. **60**, R123 (1986).
[4] G. Hautier, Am. Miglio, G. Ceder, G. Rignanese, and X. Gonze, Nature Commun. **4**, 2292 (2013).
[5] H. Kawazoe, M. Yasukawa, H. Hyodo, M. Kurita, H. Yanagi, and H. Hosono, Nature **389**, 939 (1997).
[6] N. Duan, A. W. Sleight, M. K. Jayaraj, and J. Tate, Appl. Phys. Lett. **77**, 1325 (2000).
[7] H. Yanagi, T. Hase, S. Ibuki, K. Ueda, and H. Hosono, Appl. Phys. Lett. **78**, 1583 (2001).
[8] K. Ueda, T. Hase, H. Yanagi, H. Kawazoe, H. Hosono, H. Ohta, M. Orita, and M. Hirano, J. Appl. Phys. **89**, 1790 (2001).
[9] R. Nagarajan, N. Duan, M. K. Jayaraj, J. Li, K. A. Vanaja, A. Yokochi, A. Draeseke, J. Tate, and A. W. Sleight, Int. J. Inorg. Mater. **3**, 265 (2001).
[10] R. Nagarajan, A. D. Draeseke, A. W. Sleight, and J. Tate, J. Appl. Phys. **89**, 8022 (2001).
[11] X. Nie, S.-H. Wei, and S. B. Zhang, Phys. Rev. Lett. **88**, 066405 (2002).
[12] M. Snure and A. Tiwari, Appl. Phys. Lett. **91**, 092123 (2007).
[13] D. O. Scanlon, K. G. Godinho, B. J. Morgan, and G. W. Watson, J. Chem. Phys. **132**, 024707 (2010).
[14] D. O. Scanlon and G. W. Watson, J. Mater. Chem. **21**, 3655 (2011).
[15] K. G. Godinho, J. J. Carey, B. J. Morgan, D. O. Scanlon, and G. W. Watson, J. Mater. Chem. **20**, 1086 (2010).
[16] D. O. Scanlon, A. Walsh, and G. W. Watson, Chem. Mater. **21**, 4568 (2009).
[17] A. Kudo, H. Yanagi, H. Hosono, and H. Kawazoe, Appl. Phys. Lett. **73**, 220 (1998).
[18] S. Nikitine, J. B. Grun, and M. Sieskind, J. Phys. Chem. Solids **17**, 292 (1961).
[19] D. O. Scanlon, B. J. Morgan, G. W. Watson, and A. Walsh, Phys. Rev. Lett. **103**, 096405 (2009).
[20] B. J. Ingram, G. B. Gonzalez, T. O. Mason, D. Y. Shahriari, A. Barnabe, D. Ko, and K. R. Poeppelmeier, Chem. Mater. **16**, 5616 (2004).
[21] B. J. Ingram, B. J. Harder, N. W. Hrabe, T. A. Mason, and K. R. Poeppelmeier, Chem. Mater. **16**, 5623 (2004).
[22] G. Trimarchi, H. Peng, J. Im, A. J. Freeman, V. Cloet, A. Raw, K. R. Poeppelmeier, K. Biswas, S. Lany, and A. Zunger, Phys. Rev. B **84**, 165116 (2011).
[23] H. Peng, A. Zakutayev, S. Lany, T. R. Paudel, M. d'Avezac, P. F. Ndione, J. D. Perkins, D. S. Ginley, A. R. Nagaraja, N. H. Perry, T. O. Mason, and A. Zunger, Adv. Func. Mater. **23**, 5267 (2013).
[24] M. N. Amini, H. Dixit, R. Saniz, D. Lamoen, and B. Partoens, Phys. Chem. Chem. Phys. **16**, 2588 (2014).
[25] M. Dekkers, G. Rijnders, and D. H. Blank, Appl. Phys. Lett. **90**, 021903 (2007).
[26] H. Mizoguchi, M. Hirano, S. Fujitsu, T. Takeuchi, K. Ueda, and H. Hosono, Appl. Phys. Lett. **80**, 1207 (2002).
[27] H. J. Kim, I. C. Song, J. H. Sim, H. Kim, D. Kim, Y. E. Ihm, and W. K. Choo, J. Appl. Phys. **95**, 7387 (2004).
[28] In this paper, oxygen is excluded from the scope of the term chalcogen.
[29] T. Akashi, T. Itoh, I. Gunjishima, H. Masumoto, and T. Goto, Mater. Trans. **43**, 1719 (2002).
[30] H. Hiramatsu, K. Ueda, H. Ohta, M. Hirano, T. Kamiya, and H. Hosono, Appl. Phys. Lett. **82**, 1048 (2003).
[31] K. Ueda, H. Hiramatsu, H. Ohta, M. Hirano, T. Kamiya, and H. Hosono, Phys. Rev. B **69**, 155305 (2004).
[32] H. Hiramatsu, K. Ueda, H. Ohta, M. Hirano, M. Kikuchi, H. Yanagi, T. Kamiya, and H. Hosono, Appl. Phys. Lett. **91**, 012104 (2007).
[33] D. O. Scanlon, J. Buckeridge, C. R. A. Catlow, and G. W. Watson, J. Mater. Chem. C **2**, 3429 (2014).

[34] H. Yanagi, J. Tate, S. Park, C. Park, and D. A. Keszler, Appl. Phys. Lett. **82**, 2814 (2003).
[35] H. Yanagi, J. Tate, S. Park, C. Park, D. A. Keszler, M. Hirano, and H. Hosono, J. Appl. Phys. **100**, 083705 (2006).
[36] A. Zakutayev, R. Kykyneshi, G. Schneider, D. H. McIntyre, and J. Tate, Phys. Rev. B **81**, 155103 (2010).
[37] A. Zakutayev, J. Tate, and G. Schneider, Phys. Rev. B **82**, 195204 (2010).
[38] M. L. Liu, L. B. Wu, F. Q. Huang, L. D. Chen, and I. W. Chen, J. Appl. Phys. **102**, 116108 (2007).
[39] D. O. Scanlon and G. W. Watson, Chem. Mater. **21**, 5435 (2009).
[40] G. Hautier, C. C. Fischer, A. Jain, T. Mueller, and G. Ceder, Chem. Mater. **22**, 3762 (2010).
[41] X. Zhang, V. Stevanović, M. d'Avezac, S. Lany, and A. Zunger, Phys. Rev. B **86**, 014109 (2012).
[42] A. Ohki, N. Shibata, K. Ando, and A. Katsui, J. Cryst. Growth **93**, 692 (1988).
[43] M. Grun, A. Haury, J. Cibert, and A. Wasiela, J. Appl. Phys. **79**, 7386 (1996).
[44] O. Bierwagen and J. S. Speck, Appl. Phys. Lett. **97**, 072103 (2010).
[45] J. Androulakis, S. C. Peter, H. Li, C. D. Malliakas, J. A. Peters, Z. Liu, B. W. Wessels, J. H. Song, H. Jin, A. J. Freeman, and M. G. Kanatzidis, Adv. Mater. **23**, 4163 (2011).
[46] W. Bronger and U. Hendriks, Revue de Chimie Minerale **17**, 555 (1980).
[47] A. A. Narducci and J. A. Ibers, J. Alloys Compd. **306**, 170 (2000).
[48] J. P. Perdew, K. Burke, and M. Ernzerhof, Phys. Rev. Lett. **77**, 3865, (1996).
[49] J. Heyd, G. E. Scuseria, and M. Ernzerhof, J. Chem. Phys. **125**, 224106 (2006).
[50] F. Tran and P. Blaha, Phys. Rev. Lett. **102**, 226401 (2009).
[51] D. J. Singh, Phys. Rev. B **82**, 155145 (2010).
[52] Y. S. Kim, M. Marsman, G. Kresse, F. Tran, and P. Blaha, Phys. Rev. B **82**, 205212 (2010).
[53] M. J. Li, C. L. Hu, X. W. Lei, Y. Zhou, and J. G. Mao, J. Solid State Chem. **182**, 1245 (2009).
[54] V. Stevanovic, S. Lany, X. Zhang, and A. Zunger, Phys. Rev. B **85**, 115104 (2012).
[55] M. H. Du, J. Mater. Chem. A **2**, 9091 (2014).
[56] G. Kresse and J. Furthmüller, Phys. Rev. B **54**, 11169 (1996).
[57] G. Kresse and D. Joubert, Phys. Rev. B **59**, 1758 (1999).
[58] P. Blaha, K. Schwarz, G. Madsen, D. Kvasnicka, and J. Luitz, *WIEN2k, An Augmented Plane Wave + Local Orbitals Program for Calculating Crystal Properties* (Karlheinz Schwarz, Techn. Universität Wien, Austria, 2001).
[59] S. Lany and A. Zunger, Phys. Rev. B **78**, 235104 (2008).
[60] C. G. Van de Walle and J. Neugebauer, J. Appl. Phys. **95**, 3851 (2004).
[61] H. Li, J. A. Peters, Z. Liu, M. Sebastian, C. D. Malliakas, J. Androulakis, L. Zhao, I. Chung, S. L. Nguyen, S. Johnsen, B. W. Wessels, and M. G. Kanatzidis, Cryst. Growth Des. **12**, 3250 (2012).
[62] E. A. Axtell III, J.-H. Liao, Z. Pikramenou, and M. G. Kanatzidis, Chem. Eur. J. **2**, 656 (1996).
[63] The composition is determined during refinement of the x-ray diffraction data within the Rietveld method. The method calculates the weight fraction of the components using the intensity data. For overlapping peaks such as in the case of $Cs_2Zn_3Ch_4$ and $ZnCh$ peaks, the composition determination may be problematic. In this particular case, the problem may be even more complicated by the preferred orientation of $Cs_2Zn_3Ch_4$ crystals due to the layered crystal structure.
[64] K. Biswas and M. H. Du, Appl. Phys. Lett. **98**, 181913 (2011).
[65] X. Luo, S. B. Zhang, and S. H. Wei, Phys. Rev. Lett. **90**, 026103 (2003).
[66] X. Luo, S. B. Zhang, and S. H. Wei, Phys. Rev. B **70**, 033308 (2004).
[67] S. C. Erwin, L. Zu, M. I. Haftel, A. L. Efros, T. A. Kennedy, and D. J. Norris, Nature **436**, 91 (2005).
[68] M. H. Du, S. C. Erwin, and A. L. Efros, Nano Lett. **8**, 2878 (2008).
[69] I. W. Tao, M. Jurkovic, and W. I. Wang, Appl. Phys. Letter. **64**, 1848 (1994).
[70] G. Glass, H. Kim, P. Desjardins, N. Taylor, T. Spila, Q. Lu, and J. E. Greene, Phys. Rev. B **61**, 7628 (2000).